Oxygen induced strain field homogenization in AlN nucleation layers and its impact on GaN grown by metal organic vapor phase epitaxy on sapphire: An x-ray diffraction study

J. Bläsing,[1,a] A. Krost,[1] J. Hertkorn,[2] F. Scholz,[2] L. Kirste,[3] A. Chuvilin,[4] and U. Kaiser[4]
[1]*Institute of Experimental Physics, Otto-von-Guericke-University Magdeburg, Universitätsplatz 2, D-39016 Magdeburg, Germany*
[2]*Institute of Optoelectronics, Ulm University, Albert-Einstein-Allee 45, D-89081 Ulm, Germany*
[3]*Fraunhofer-Institute of Applied Solid State Physics, Tullastraße 72, D-79108 Freiburg, Germany*
[4]*Central Facility of Electron Microscopy, Ulm University, D-89069 Ulm, Germany*

(Received 6 October 2008; accepted 12 December 2008; published online 3 February 2009)

This paper presents an x-ray study of GaN, which is grown on nominally undoped and oxygen-doped AlN nucleation layers on sapphire substrates by metal organic vapor phase epitaxy. Without additional oxygen doping a trimodal nucleation distribution of AlN is observed leading to inhomogeneous in-plane strain fields, whereas in oxygen-doped layers a homogeneous distribution of nucleation centers is observed. In both types of nucleation layers extremely sharp correlation peaks occur in transverse ω-scans which are attributed to a high density of edge-type dislocations having an in-plane Burgers vector. The correlation peaks are still visible in the (0002) ω-scans of 500 nm GaN which might mislead an observer to conclude incorrectly that there exists an extremely high structural quality. For the undoped nucleation layers depth-sensitive measurements in grazing incidence geometry reveal a strong thickness dependence of the lattice parameter a, whereas no such dependence is observed for doped samples. For oxygen-doped nucleation layers, in cross-sectional transmission electron microscopy images a high density of stacking faults parallel to the substrate surface is found in contrast to undoped nucleation layers where a high density of threading dislocations is visible. GaN of 2.5 μm grown on top of 25 nm AlN nucleation layers with an additional *in situ* SiN mask show full widths at half maximum of 160″ and 190″ in (0002) and (10–10) high-resolution x-ray diffraction ω-scans, respectively. © *2009 American Institute of Physics*. [DOI: 10.1063/1.3074095]

I. INTRODUCTION

Group III-nitrides have a strong impact in the semiconductor industry because of their potential in applications such as light-emitting diodes and laser diodes as well as high-temperature/high-power electronic devices. In spite of rapid progress in the development of these nitride-based devices in the last years, the growth of GaN is still problematic as III-nitride-based semiconductor caused by the fact that it is usually grown on foreign substrates such as sapphire (Al_2O_3) or silicon carbide (SiC). Compared to SiC, sapphire has its advantages, e.g., the lower price and its superior material quality. In order to overcome obstacles such as the lattice mismatch and the comparatively larger thermal expansion coefficient of wurtzite GaN than sapphire, a low-temperature nucleation layer (NL) consisting of AlN (Ref. 1) or GaN (Ref. 2) has to be applied as initial growth step before the deposition of the GaN material. Both types of NLs are widely used and indispensable to grow high quality GaN on sapphire. Recently, oxygen doping during the deposition of an AlN nucleation was established to achieve high quality GaN layers.[3,4] We studied such layers by x-ray diffraction, transmission electron microscopy (TEM), and secondary ion mass spectroscopy (SIMS) to reach a better understanding of the underlying nucleation mechanism.

II. EXPERIMENTAL

The samples were grown by metal organic vapor phase epitaxy (MOVPE) in an AIXTRON 200/RF-S single wafer reactor. 2 in. *c*-plane epiready sapphire wafers slightly miscut by about 0.3° toward the *a*-plane were used as substrates. Before deposition, the substrates went through *in situ* annealing[5] at a temperature of 1200 °C for 10 min in a hydrogen atmosphere. Oxygen doping of the AlN nucleation was done with a mixture of 0.3% oxygen in nitrogen. Standard precursors trimethylaluminum (TMAl), trimethylgallium (TMGa), and high purity ammonia were used to deposit the NL and the nominally undoped GaN layer, respectively. The carrier gas was Pd-diffused hydrogen. Further details about the appropriate growth conditions of the samples are given elsewhere.[4]

As this paper is concentrating on the evaluation of the crystal properties by x-ray diffraction, four sample series layers of the following characteristics were grown: nominally undoped and oxygen-doped AlN NLs of different thicknesses as well as the corresponding NLs with additional 500 nm nonintentionally doped GaN buffer. In the following the

[a]Author to whom correspondence should be addressed. Electronic mail: juergen.blaesing@ovgu.de.

samples are described as follows: e.g, AlN_25 or AlN:O_25 stand for an undoped or doped AlN NL of 25 nm thickness, respectively, and GaN/AlN_25 or GaN/AlN:O_25 for the corresponding NLs with additional 500 nm GaN on top.

The oxygen concentration in the AlN NLs was analyzed by SIMS. With this technique, depth profiles were recorded using 5 keV Cs primary ions at an impinging angle of 45° and detecting secondary ions of the dopant O^-. The AlN matrix was analyzed by detecting Al_2^- as well as Al_2N^-. The widths of the quadratic craters were 250 μm. An electron beam irradiation was applied for charge neutralization. Relative sensitivity factors (RSFs) were used for quantitative calibration of the secondary ion intensity of O^-.[6] The RSFs of the doping O^- normalized to the matrix of Al_2^- and Al_2N^- were derived from an implanted standard sample. From the SIMS measurements oxygen was found to be homogeneously distributed in the doped AlN NLs apart from surface and interface effects with $\sim 8\times 10^{21}$ cm^{-3} corresponding to about 10% oxygen in the AlN NLs. In nominally undoped samples the background concentration is around 10^{20} cm^{-3}.

The local crystal structure of the layers was evaluated by TEM. Cross-sectional samples were prepared by standard method including cross cutting, mechanical grinding, dimpling, and final polishing by Ar ion beam at 5 keV. The prepared samples were investigated using Titan 80–300 (FEI, Netherlands) microscope operated at 300 kV. Diffraction contrast images (in bright field and dark-field modes) were used for qualitative evaluation of concentration and types of defects. High-resolution images (not shown here) revealed local atomic arrangement in the vicinity of defective regions.

In order to evaluate the structural properties, the samples were investigated systematically by ω and $\theta/2\Theta$ scans parallel and perpendicular to the *c*-axis growth direction around the (000l) and (10–10) Bragg reflections, respectively. For the former, a high-resolution Seifert XRD 3003 diffractometer equipped with a multilayer mirror, Ge(220) fourfold monochromator, and an analyzer crystal in combination with Cu $K\alpha$ radiation was used. Reciprocal space maps (RSMs) were performed with a Bruker D8 diffractometer equipped with a rotating Cu anode, primary monochromator, and a Vantec 2000 area detector with an area of 14×14 cm^2 and a resolution of about 50″ in ω and 2Θ. Grazing incidence in-plane investigations (GIID) on the (10–10) Bragg reflection were performed with the help of a modified Seifert/FPM URD6 diffractometer enabling also depth-sensitive measurements at high intensity. For this purpose the conventional x-ray tube was mounted vertically upside down thus the full length of line focus (12 mm) being located horizontally and parallel to the sample surface (instead of the 1 mm point focus). By this the intensity at the sample was enhanced by more than an order of magnitude enabling thin films (<10 nm) to be investigated with respect to their in plane lattice parameter. Moreover the whole x-ray tube could be moved vertically. Depth sensitivity was obtained via the different acceptance angles of the sample for the incoming divergent light.

III. X-RAY RESULTS

A. Θ/2Θ-scans at the (0002) Bragg reflection

First, we compare the AlN NLs grown with and without additional oxygen with thicknesses of 25, 70, and 140 nm samples. Figures 1(a) and 1(b) show the corresponding $\Theta/2\Theta$ scans around the AlN (0002) reflection. For both sets of samples a central AlN(0002) peak with an asymmetric finite thickness interference fringe structure is visible only for the 25 and 70 nm samples. The interference fringes are smeared out for the thickest sample indicating a rougher surface. Moreover, the 120 nm sample with oxygen is not single crystalline because the (10–11) reflection at 37.8° appears. The asymmetric background structure with higher intensity at the low angle side is typical for a strong compressive, homogeneous strain profile in growth direction. With increasing thickness and relaxation, the (0002) peak systematically shifts from $2\Theta=35.8°$ to 36.1°, i.e., toward the position of relaxed AlN (36.03°). Depth-sensitive grazing incidence measurements at the (10–10) reflection clearly revealed also an in-plane strain gradient (see Sec. III). Remarkably, for all samples grown with additional oxygen, the 2Θ values are higher by about 0.1°, whereby the whole structure looks broadened due to the less pronounced interference fringes and the AlN NLs seem to be worse than without oxygen. We attribute the shift to the large amount of oxygen ions (O^-) replacing nitrogen atoms. Simulations (commercial software: LEPTOS, Bruker AXS) of the measured diffraction curves were performed to get an idea of the strain involved. As an example in Fig. 1(c) the result for the 25 nm NL with oxygen is shown. Reasonable agreement was obtained by dividing the layer in two parts of 9 and 16 nm thicknesses. The first 9 nm were simulated with an exponentially strain-graded AlN with compressive strains of -0.59% at the sapphire interface and -0.533% at 9 nm AlN; the next 16 nm were simulated with a constant (-0.533%) compressively strained AlN.

Figure 1(d) shows a (0002) RSM of the 25 nm AlN NL showing a sharp vertical peak, which will be called correlation peak in the following. The peak is running strictly in the q_z direction, indicating its origin to be located parallel to the surface in real space. Due to its high intensity, it cannot be attributed solely to a surface truncation rod. At both sides of the correlation peak strong diffuse scattering is visible. The two asymmetrically located bumps are due to a detector streak as shown in Fig. 2(d). It is caused by an electronic artifact of the area detector and is therefore not of interest here.

Figures 2(a) and 2(b) show the corresponding $\Theta/2\Theta$ measurements on 25, 40, and 70 nm AlN NLs with additional 500 nm GaN on top. Now the diffractograms are dominated by the GaN(0002) reflection at $2\Theta=34.5°$ with a symmetric background on both sides and the additional AlN(0002) reflection around 36°. It is apparent that the best GaN is obtained on 25 nm AlN with oxygen doping, as indicated by the well pronounced finite thickness interference fringes from both the AlN NL and the total layer stack in this sample as revealed in the zoomed image 2c. In Fig. 2(d), a (0002) RSM of the 500 nm GaN/AlN:O_25 is shown. The picture is dominated by the central GaN peak with the dif-

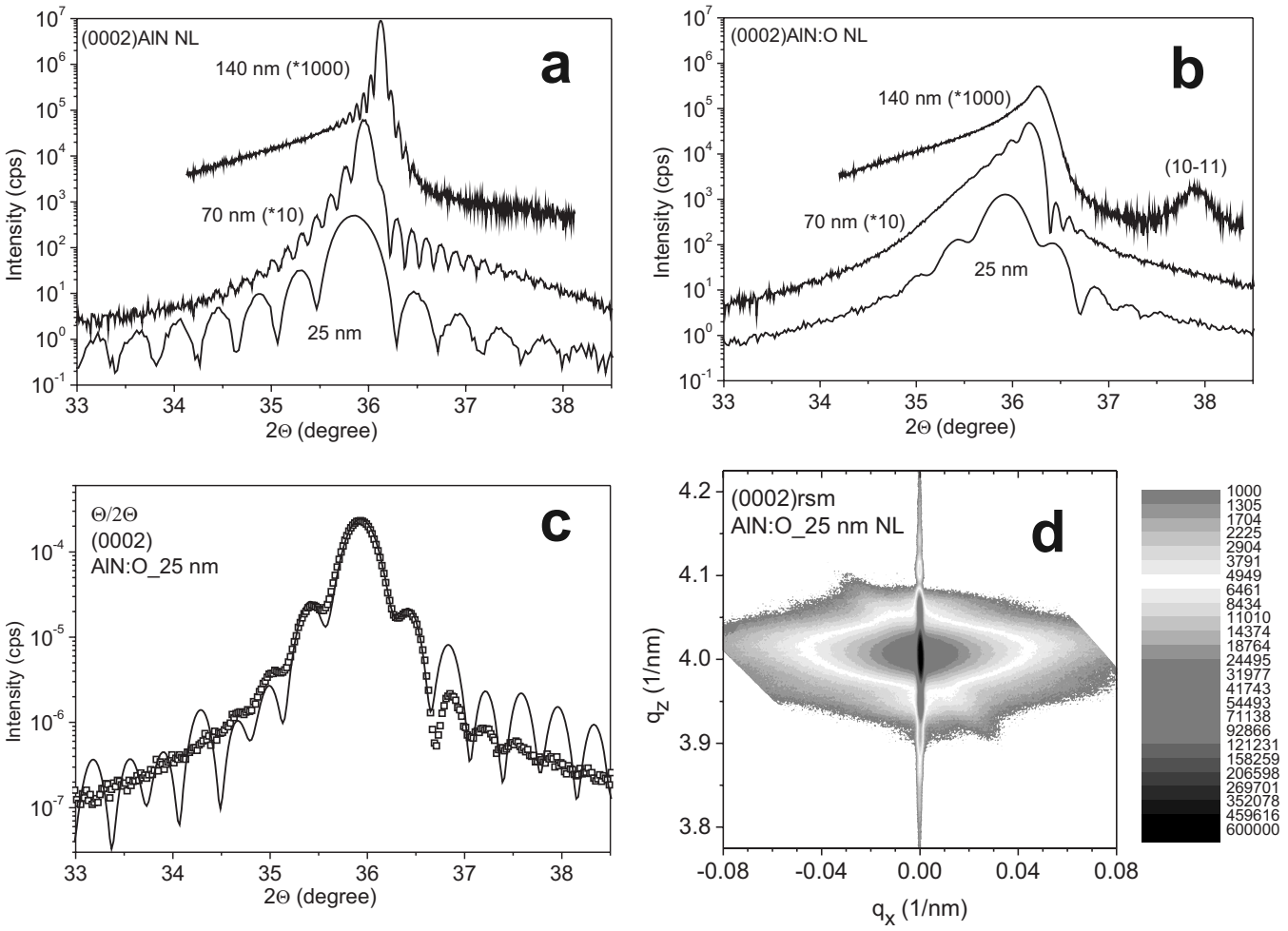

FIG. 1. Θ/2Θ-scans at (0002) of AlN_25, AlN_70, and AlN_140 (a); Θ/2Θ-scans at (0002) of AlN:O_25, AlN:O_70, and AlNO_140 (b); measurement and simulation of AlN:O_25 (c); RSM around (0002) of AlN:O_25 (d).

fuse background scattering on both sides. On top of it, the scattering intensity from AlN and its diffuse background are visible. The feature between the two main peaks is an interference structure that mirrors the thickness of the AlN layer. It is more clearly visible in the Θ/2Θ scans. The sharp vertical streak running in the q_z direction at $q_x=0$ ($\omega=\Theta$) stems from a correlation peak (see Sec. III B) due to the defects in the layer, which must be oriented perpendicular to it. Note that the vertical peak is not restricted to AlN but extends to the GaN layer. Without the knowledge of this fact, in a transverse ω-scan, such a peak would be misleadingly interpreted as an extremely small tilt, i.e., as a high structural quality attribute in terms of perfectly aligned c-axes of the GaN crystallites. Further details will be discussed in Sec. III C. Finally, the inclined streak is again caused by the detector and therefore not of interest here.

B. ω-scans at (000l), correlation peak

Next, we performed (000l) ω-scans on the different AlN layers in order to obtain information on the tilt and its distribution as well as on correlation length as determined by the crystallite size. In Figs. 3(a) and 3(b) the results on the (0002) Bragg reflections are displayed. All diffraction patterns look very similar, consisting of a two-component contribution with an extremely sharp line at the AlN(0002) position and a broad diffuse scattering with much lower (<10) peak intensity. The full with at half maximum (FWHM) of the sharp peak of the 25 nm samples is 11″, being the resolution limit of the diffractometer setup and/or the curvature of the sample. Next, we grew a sample series with such NLs and additional 500 nm GaN on top and did similar measurements. In spite of the high GaN growth temperature (1090 °C), the overall diffraction patterns remained the same as already revealed by the RSM in Fig. 2(d). Very similar observations have been reported for ErAs/GaAs(001),[7] AlN/sapphire,[8] GaN/sapphire,[9] ZnO/sapphire,[10] $SrBi_2Nb_2O_9/SrTiO_3$ (SBN),[11] and Nb/Al_2O_3.[12] Such diffraction patterns can be explained by a long-range as well as a short-range order in the epitaxial systems.[7,11,13] The origin of the diffuse scattering can be either due to the angular spreading of the c-axis (tilt) or small crystallite diameters and spatial correlations in dislocation networks, i.e., a short in-plane correlation length parallel to the substrate, or both. In the symmetric geometry considered here, in the case of correlation lengths being responsible, the angular width of the diffuse scattering should narrow with higher order reflections because of the higher q-vector transform. The more general case is discussed, e.g., in the book of Als-Nielsen and McMorrow[14] and in Ref. 11. The description is essentially

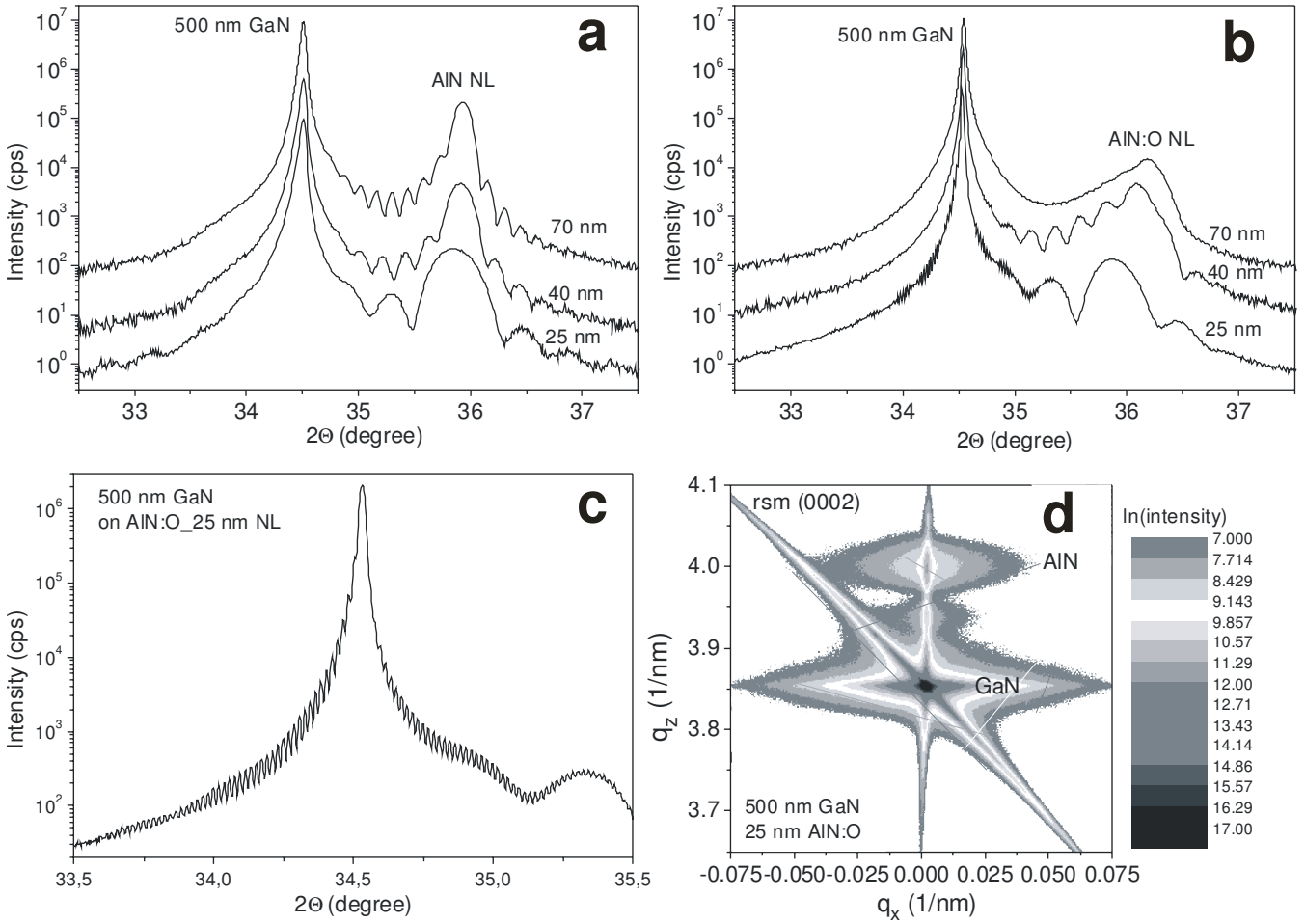

FIG. 2. (Color online) Θ/2Θ-scans at (0002) GaN/AlN_25, AlN_40, and AlN_70 (a); Θ/2Θ-scans at (0002)GaN/AlN:O_25, AlN:O_40, and AlN:O_70 (b); zoomed image for (0002)GaN/AlN:O_25 (c); and RSM around (0002)GaN/AlN:O_25 (d).

the same as for x-ray reflectivity. In Ref. 14, it is shown that the scattering from a surface (or interface) where the height fluctuations are correlated consists always of two components: As a function of an in-plane scattering vector, the scattered intensity has a sharp specular component superimposed on a diffuse background. For diffraction the origin of the sharp peak (correlation peak) can be attributed to the dislocation networks, which are seen by the x rays as a long-range ordered correlated system.[11,13] In our case the planes of disturbance, due to the inhomogeneous strain fields of the defects, must be parallel to the substrate because the streak is running strictly in the *c*-axis direction. As has been pointed out in Ref. 9, such defects could be, for example, inversion domain boundaries or pure edge-type threading dislocations with Burgers vectors in the substrate-film interface.

In Figs. 4(a) and 4(b) the symmetric *ω*-scans of the higher order reflections (0002), (0004), and (0006) are shown for the 70 nm AlN films without and with additional oxygen, respectively. In the latter case [Fig. 4(b)] we observe a very similar structure as given by Metzger *et al.*[8] in Fig. 2; the shape and angular width of the diffuse scattering components remain the same, independent of the diffraction order,

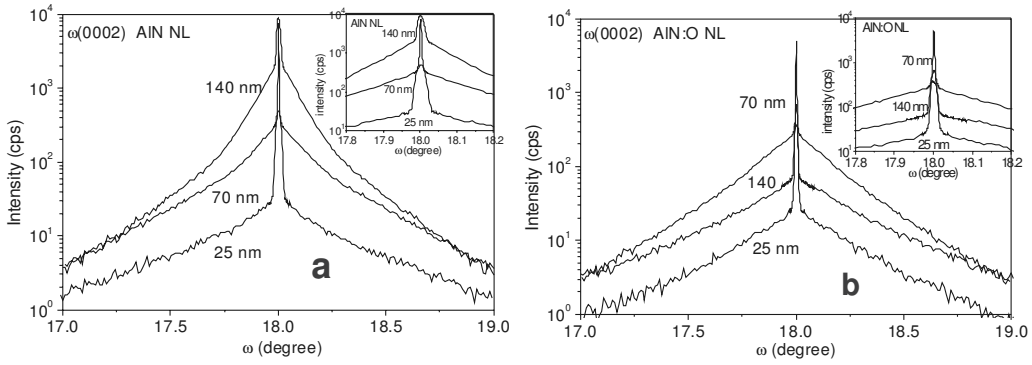

FIG. 3. *ω*-scans at (0002)AlN_25, AlN_70, and AlN_140 (a); *ω*-scans at (0002)AlN:O_25, AlN:O_70, and AlN:O_140 (b).

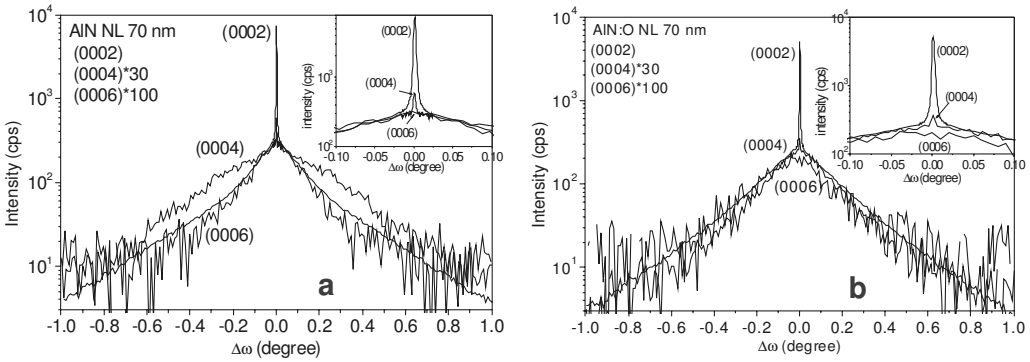

FIG. 4. ω-scans at (0002), (0004), and (0006) AlN_25 (a); ω-scans at (0002), (0004), and (0006) AlN:O_25 (b).

proving that the diffuse scattering is due to tilt. The sharp line vanishes for the (0006) reflection due to the nonperfectness in the correlation part of the scattering, i.e., the disorder in the distance correlation of the underlying defect structure and the finite thickness of the films.[12] In contrast, a different behavior is observed for the 70 nm sample without oxygen. Here, the sharp line vanishes as well; however, the diffuse component first broadens from (0002) to (0004) and then shrinks for (0006) below the value of the (0002) reflection, where its shape changes from concave via convex to concave. A similar behavior was observed and explained with SBN by Boulle *et al.*[11] in terms of inhomogeneous, localized strain fields caused in their case by imperfect stacking faults. They showed that neither a Gaussian nor a Lorentzian probability density function can explain such behavior; instead the more general Lévy-stable distribution suitable for the description of inhomogeneous strain fields has to be applied, which can reproduce all types of shapes with one single function. From a comparison with the work of Boulle *et al.*, we conclude that the AlN NLs grown with oxygen do not contain inhomogeneous localized strain fields, whereas the AlN NLs without oxygen do. In other words, the oxygen ions homogenize the NL with respect to the strain distribution, i.e., they guarantee a homogeneous distribution of the stress-releasing edge dislocations. The origin of the inhomogeneous strain fields in the oxygen-free NLs most probably is a trimodal AlN nucleation on sapphire as discussed below.

In Figs. 5(a) and 5(b), the ω-scans of 500 nm GaN(0002) which has been grown on top of AlN NLs of different thicknesses (25, 40, and 70 nm) without and with oxygen are shown, respectively. All samples were measured with the same setup, i.e., the absolute intensities are comparable. We observe a drastic difference between the diffraction patterns of the two series. Without oxygen the highest maximum intensity (94.000 cps) and lowest halfwidth (338 arc sec) is obtained with the 25 nm AlN NL, followed by the 70 nm NL (same intensity, 421 arc sec), and finally the 40 nm NL (66.000 cps, 648 arc sec). A strong diffuse background (6.000 cps) is observable on all three samples. In contrast, the structural properties for the samples grown on the oxygen-containing NLs systematically vary with the thickness, and the scattered intensity is much more concentrated in the central peak. For the 25 nm NL we obtain 1.500.000 cps at 0.015°, followed by the 40 nm NL with 240.000 cps at 0.087°, and finally values of 108.000 at 0.203° for the 70 nm NL. However, care should be taken when interpreting these values. The extremely low value for the half width of GaN/AlN:O_25 is not due solely to structural quality but also due to the correlation peak originating in the AlN NL. Therefore, in order to separate between tilt and coherence length, in addition, the higher order GaN(0004) and (0006) reflections were measured (Fig. 6).

Clearly, the shape of the (0002) reflection consists of two contributions: as already discussed with the RSM [Fig. 2(d)], the correlation peak of the AlN NL extends to the GaN and is visible as a sharp peak superimposed on a broad background. Therefore it is not correct to take the FWHM of the correlation peak as a direct measure for the structural quality in terms of tilt. Instead, both components should be separated in a broad background and a sharp peak. It should be mentioned that none of the (000l) reflections could be fitted with Gauss-

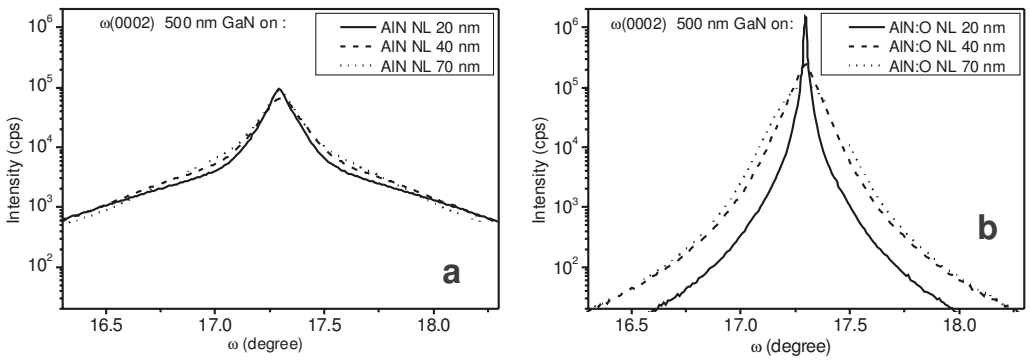

FIG. 5. ω-scans at (0002) GaN/AlN_25, GaN/AlN_40, and GaN/AlN_70 (a); ω-scans at (0002) GaN/AlN:O_25, GaN/AlN:O_40, and GaN/AlN:O_70 (b).

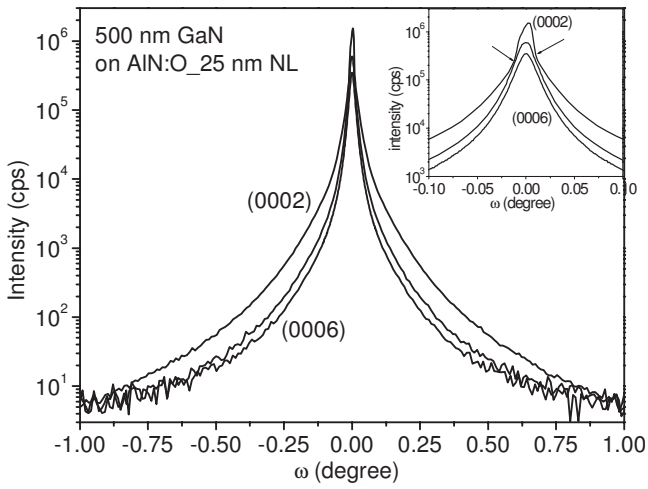

FIG. 6. ω-scans at (0002), (0004), and (0006) GaN/AlN:O_25. The inset shows an enlarged view of the (0002) measurements revealing the two-shape behavior. The arrows mark the transition from diffuse to correlated intensity.

ian, Lorentzian, or pseudo-Voigt profiles, i.e., we have the intermediate case as discussed by Boulle.[11] For the higher order reflections, only the background is visible with FWHMs of 64″ and 68″ for the (0004) and (0006) Bragg reflections, respectively. However, it cannot be ruled out that there is no contribution of the correlation peak at all. In any case, it is reasonable to assume that the FWHM of the (0002) reflection should be not smaller than 64″ because, in general, the FWHM should decrease with increasing scattering order. In contrast, from the measured (0002) curve, one obtains a FWHM of only 47″. Therefore we conclude that the quality of the material is generally overestimated when correlation peaks come into play. The shape of the ω-background is not pseudo-Voigt-like (from Gaussian to Lorentzian) and depends on the order in ω (degree) as well as in q_x (1/nm) (not shown here). It means that the GaN neither complies with the pure tilt case nor with the case of pure in-plane particle size and represents a different system of anisotropic inhomogeneous strain distribution like AlN:O NL.

C. Grazing incidence measurements: ω-scans at the (10–10) Bragg reflection

In the following we discuss the azimuthally in-plane rotation (twist) behavior of the same AlN NLs (25, 70, and 140 nm) grown with and without oxygen. For this purpose, (10–10) ω-scans were performed at an incoming angle of 0.3° corresponding nearly to the angle of total external reflection condition.

In Figs. 7(a) and 7(b) the results are shown for AlN without and with oxygen, respectively. For the latter [Fig. 7(b)], a normal behavior is observed with a very broad angular intensity distribution ranging from 1.8° (70 nm) over 1.9° (25 nm) to 2.9° (140 nm), whereby the corresponding maximum intensity varies as ~10:5:1. All traces can be well described by a one Gaussian distribution function. Surprisingly, a completely different picture is found for the oxygen-free NLs [Fig. 7(a)]. Here we observe an extremely broad hutlike scattering distribution for the 25 nm sample and a camelback-shaped distribution for the other two. All curves can be fitted assuming three Gaussians each [Figs. 7(c) and 7(d)]. The hutlike curve can be fitted with a strong

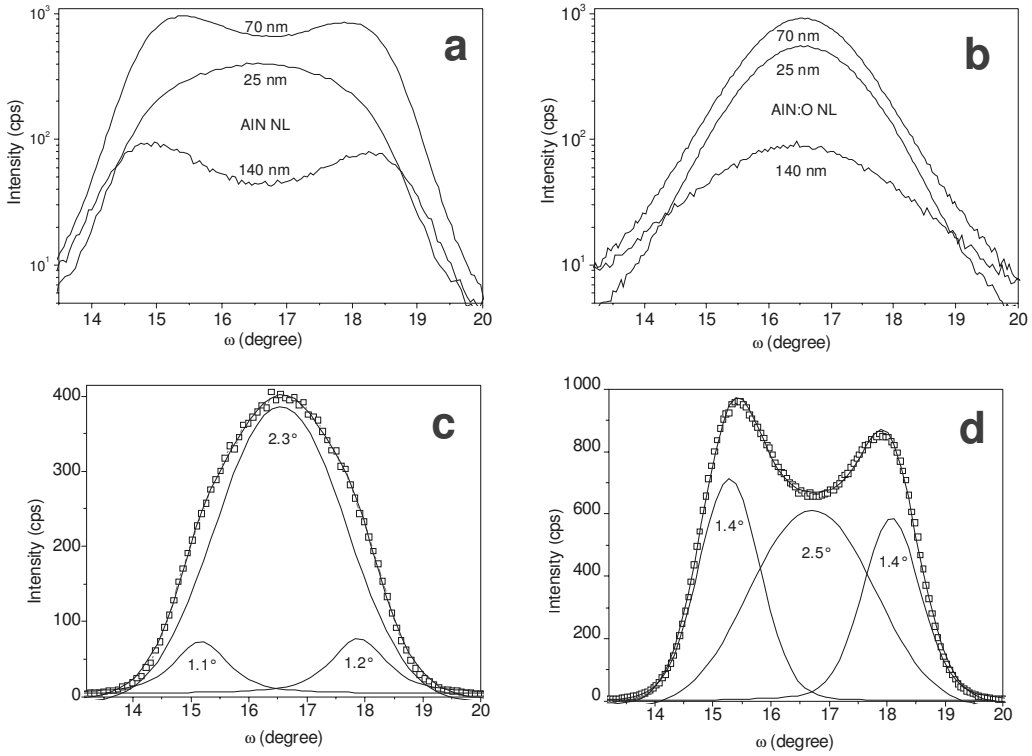

FIG. 7. ω-scans at (10–10)AlN_25, AlN_70, and AlN_140 (a); ω-scans at (10–10)AlN:O_25, AlN:O_70, and AlN:O_140 (b); simulation with three Gaussians to (10–10)AlN_25 (c) simulation with three Gaussians to (10–10)AlN_70 (d).

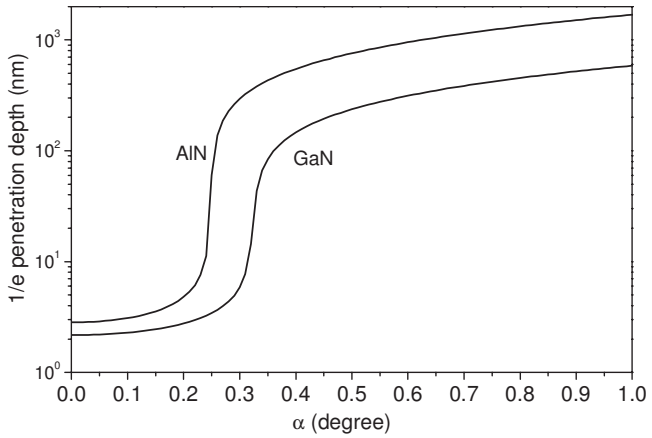

FIG. 8. Calculated $1/e$ intensity penetration depth as a function of the incoming angle α for Cu $K\alpha$-radiation in AlN and GaN.

central peak with a FWHM of 2.3° and two weaker peaks of similar intensity and FWHM of 1.4°, each located nearly symmetrically at the low (1.37°) and high (1.29°) angle sides of the main peak. The same holds for the camelbacklike distributions. The fit for the 70 nm sample yields a central peak with FWHM of 2.5° and two side peaks with FWHMs of 1.4° each separated by −0.90° and +0.92° from both sides. Obviously, the AlN crystallites do not nucleate with a statistical in-plane rotational distribution but preferentially adopt three nucleation sites resulting in a trimodal distribution of the twist values which we believe is the origin for the inhomogeneous strain fields revealed in ω-scans of the diffuse scattering around the (000l) Bragg reflections. Cross-sectional high-resolution TEM images confirm the existence of multiple nucleation sites of AlN on sapphire (not shown here).

The trimodal distribution is not transferred to the 500 nm GaN layers on top. For these we measure Gaussian-like twist distributions with FWHMs around 0.35° for all oxygen-free samples; in contrast, the corresponding values for the samples with an oxygen-containing AlN NL broaden systematically from 0.3° (25 nm) through 0.46° (70 nm), to 0.5° (140 nm) (not shown here).

The existence of vertical strain fields in the AlN NLs was already revealed by the $\Theta/2\Theta$ measurements at the (0002) Bragg reflections shown in Figs. 1(a)–1(c). Direct access to the in-plane strain evolution is provided by depth-sensitive grazing incidence in-plane x-ray diffraction GIID $\Theta/2\Theta$ measurements at the (10–10) Bragg reflection by varying the incoming angle α of the x-ray beam with respect to the sample surface; with increasing α_i the penetration depth of the x rays increases. For a general discussion on this topic see, e.g., Refs. 15 and 16.

In Fig. 8, the calculated intensity penetration depth of the intensity in AlN and GaN for Cu $K\alpha$ radiation is shown. The critical angles for total external reflection are 0.25° and 0.325° for AlN and GaN, respectively.

In Fig. 9(a), the result of such a measurement at the 70 nm AlN NL without oxygen is shown. The vertical line marks the diffraction angle of relaxed AlN. Starting with an incoming angle of 0.2° below the critical one of total external reflection, the measurements were performed in steps of $\Delta\alpha$=0.1°. For angles below the critical one, the amplitude of the evanescent wave decays at a short distance into the sample, typically 5 nm. In this very near surface region, the AlN is nearly relaxed. At the critical angle the penetration depth is strongly increased by roughly an order of magnitude and the x-ray beam penetrates nearly the whole layer; at this position we observe a shift of the peak maximum toward higher scattering angles by 0.1° corresponding to a strain $\Delta a/a$ of 0.3%. With increasing penetration depth, up to α =0.5° the peak maximum stays constant and the shape remains nearly the same. Hence, close to the AlN/sapphire interface, we observe a strong gradual shift of the peak maximum accompanied by a drastic broadening of the whole structure. The final position of the maximum corresponds to a strain of 1.6%.

In Fig. 9(b), the corresponding measurement for the 70 nm oxygen-doped layer is shown. In addition to the AlN maxima, an additional K_β peak stemming from sapphire is visible because the optical adjustment was done with respect to the maxima, which are at slightly different angles [see Figs. 7(a) and 7(b)]; this peak is not of interest here. Again, the vertical line marks the position of relaxed AlN. In contrast to Fig. 7(a), only a marginal shift of the maxima is visible when scanning from the surface to the interface. In other words, the strain relaxation process for the oxygen-doped NL took place in a completely different way and already much more effective close to the interface than without oxygen and the in-plane strain distribution is much more homogeneous than in the former one.

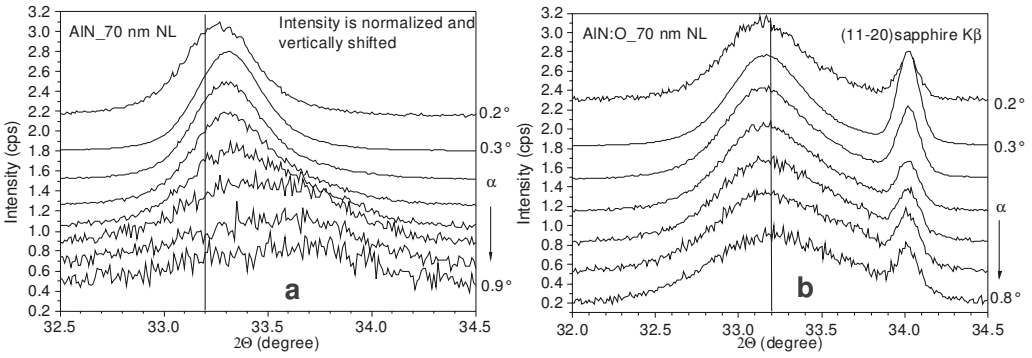

FIG. 9. Depth dependent (10–10) $\Theta/2\Theta$-measurements at AlN_70 (a) and AlN:O_70 (b).

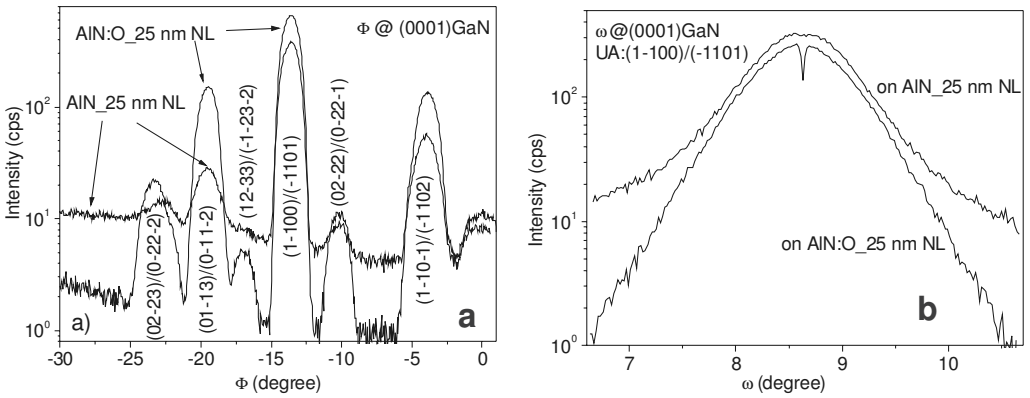

FIG. 10. Multiple reflection (Umweganregung) at the primary forbidden (0001) Bragg reflection in GaN/AlN_0.25 and GaN/AlN:O_0.25 as a function of azimuthal rotation Φ for a fixed detector angle 2Θ (a); ω-scans at the internal reflection pair (1–100)/(−1101) for the same samples (b).

D. X-ray multiple diffraction (Umweganregung)

X-ray multiple diffraction is rarely applied for the purpose of characterization of wurtzite-type layers. However, some years ago, we have shown that this technique can be used as a quick and nondestructive tool for a simultaneous characterization of their structural quality in terms of tilt and twist. In particular, the normally forbidden (0001) Bragg reflection is well suited for an internal excitation of the double reflection pair (1–100)/(−1101) as the two Bragg reflections bear information on pure twist and pure tilt, respectively.[17]

For such measurements, the detector was set at exactly the Bragg position of the primary forbidden (0001) reflection at $2\Theta = 17.075°$ and the sample rotated azimuthally around the [0001] *c*-axes. Figure 10(a) shows the result of such a measurement as a function of the azimuthal rotation Φ for the (0001) reflection at samples GaN/AlN_25 and GaN/AlN:O_25 on a logarithmic scale. The position $\Phi = 0$ corresponds to the (10–10) azimuth. The six pairs of visible multiple reflections could all be identified as indicated in the figure. The striking difference in the GaN quality is very clear. In the case of the oxygen-doped NL, the background intensity is drastically reduced by nearly an order of magnitude and all peaks exhibit much higher intensity than without oxygen doping. Next, we choose the reflection pair with highest intensity (1–100)/(−1101) at $\Phi = -13.618°$ and performed an ω-scan around it for both samples, expecting a contribution of in-plane and symmetric ω broadenings dependent on the reflection pair chosen. The results are displayed in Fig. 10(b). Again, GaN/AlN:O_25 shows a reduced background and smaller FWHM. More striking is the sharp dip at the maximum, where the intensity is reduced. We attribute this to the anomalous dynamical absorption from the correlation part of the (0001) Bragg reflection, proving indeed the existence of the correlation in the case of strong disorder as well. To the best of our knowledge, this is the first time such an effect has been observed.

Summarizing these findings we conclude that 500 nm GaN with ω-FWHM values of the subgrains around 65″ can be grown by MOVPE on an oxygen-doped AlN NL with an optimized thickness of 25 nm. But this low "tilt" values are attributed to a high density of homogeneously distributed pure edge-type threading dislocations with an in-plane Burgers vector.[18] The homogeneity is accomplished via oxygen doping of AlN. On the other hand the individual crystallites of such samples exhibit an extremely high azimuthal rotation with twist values > 1000 in. A high density of edge-type dislocations manifests itself as a sharp correlation peak in x-ray (0002) ω-scans whose halfwidth is only limited by the optical setup and in the case of wafer bowing by the curvature. It should be stressed that the correlation peak does not infer a high structural quality, in general, and its halfwidth can be smaller than that calculated for perfect thick crystals in the framework of the dynamical theory of x-ray diffraction. The result obtained in dynamical theory is usually called a rocking curve and not an ω-scan; the latter being a cut through the rocking curve landscape via the usage of an analyzer crystal in front of the detector. In the case of very thin films considered here the rocking curve width is determined by the finite thickness of the layer. Typical GaN buffer layers using AlN:O NLs for further growth of device structures have a thickness of ~2.5 μm and reach FWHMs for ω-scans of (0002) and (10–10) FWHMs of 160″ and 190″, respectively.[4]

Comprehensive TEM measurements which have been performed on these samples confirm the interpretations of the x-ray results. This is illustrated with the following example: The most striking difference between the AlN NLs without [AlN _70, Fig. 11(a)] and with oxygen [AlN:O_70, Fig. 11(b)], however, is the appearance of a high density of stacking faults parallel to the interface in the former case, whereas for the undoped sample mainly vertical defect structures are visible as shown in the cross-sectional dark-field images [Figs. 11(a) and 11(b)]. It can be concluded that pure edge dislocations serve as the main strain relaxing mechanism via the generation of stacking faults and result in a homogeneous *a* lattice parameter distribution across the layer thickness, whereas in the oxygen-free sample mostly threading dislocations appear involving an inhomogeneous in-plane strain distribution. In both cases there is, however, a strong *c*-lattice parameter variation (see Fig. 1). Both NLs exhibit a strong surface roughness (see Fig. 11). Nevertheless, unexpectedly, distinct finite thickness interference fringes have been observed in x-ray $\Theta/2\Theta$ measurements, as shown above, and also in large-scale x-ray reflectivity measurements (not shown here), normally typical for high qual-

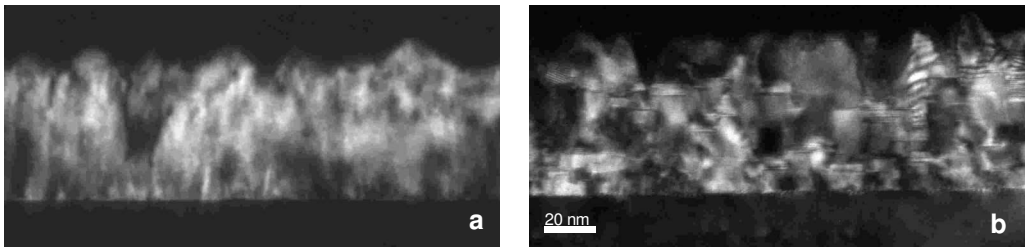

FIG. 11. Cross-sectional TEM dark-field images of AlN_70 (a) and of AlN:O_70 (b) showing single crystalline NLs with a strong surface roughness in both cases. Inside of the films for AlN (a) primarily a dense vertical defect structure and for AlN:O (b) mostly horizontal stacking faults are visible.

ity thin films. These can only be understood in terms of diffraction on crystallographically correlated surface regions with the same thickness, whereas the TEM pictures show the entire real structure.

IV. SUMMARY

Recently, oxygen doping during MOVPE growth of an AlN NL on *c*-sapphire was found to be helpful to achieve high quality GaN layers.[3,4] To evaluate the origin of this effect we performed an x-ray study of undoped and oxygen-doped high-temperature AlN NLs alone and together with a 500 nm GaN layer on top. Without intentional oxygen incorporation a trimodal in-plane rotational distribution (twist) of AlN crystallites and associated inhomogeneous in-plane strain fields in the AlN layers are observed. In contrast, additional oxygen incorporation of ~10% leads to a homogeneous statistical twist distribution. Cross-sectional electron transmission microscopy revealed a high density of stacking faults parallel to the substrate surface in the oxygen-doped samples and a high density of threading dislocations in the undoped NLs. In transverse ω-scans at the (0002) Bragg reflection in both types of NLs extremely sharp correlation peaks occur in q_z-direction which are attributed to a high density of spatial correlated edge-type dislocations with in-plane Burgers vector and associated stacking faults. The visibility of the correlation peak depends on the amount of correlation. With increasing nonperfectness the correlation peak vanishes with increasing reflection order. Under certain conditions the correlation behavior of the AlN buffer layer is adopted by a thick GaN layer on top but should not be interpreted as a better structural quality attribute of the latter one.

As a general rule ω-scans are expected to be of Gaussian shape in the case of usual isotropic mosaicity. If this is not the case higher order reflections should be measured in order to check for the presence of correlation peaks. For example, 500 nm GaN grown on top of 25 nm AlN NLs show a FWHM as low as ~47 *in*. in (0002) ω-scans when the correlation peak is taken into account. However, the higher order reflections (0004) and (0006) have 64″ to 68″ although they should be smaller than in (0002).

Depth dependent grazing incidence measurements reveal a strong variation in the lattice parameter a in the case of undoped NLs, whereas this parameter is nearly constant in the doped layers, i.e., the doping influences the vertical strain distribution inside of the ALN NLs.

In addition, anomalous dynamical absorption from the correlation part of the (0001) Bragg reflection (Umweganregung) proving the existence of the correlation in the case of strong disorder has been observed for the first time.

Applying oxygen doping in 25 nm AlN NLs and inserting in addition a SiN *In-situ* mask, for 2.5 μm GaN (not shown here) best ω-values for (0002) and (10–10) of 160″ and 190″ were obtained, respectively.

ACKNOWLEDGMENTS

This research was partly funded by Osram Opto Semiconductors and the Bundesministerium für Bildung und Forschung (BMBF). The authors would like to thank T. Fuchs and M. Grimm for expert assistance in the SIMS analysis and Quincy Liu for critical reading of the manuscript.

[1]H. Amano, N. Sawaki, I. Akasaki, and Y. Toyoda, Appl. Phys. Lett. **48**, 353 (1986).
[2]S. Nakamura, Jpn. J. Appl. Phys. **30**, L1705 (1991).
[3]B. Kuhn and F. Scholz, Phys. Status Solidi A **188**, 629 (2001).
[4]J. Hertkorn, P. Brückner, S. B. Thapa, T. Wunderer, F. Scholz, M. Feneberg, K. Thonke, R. Sauer, M. Beer, and J. Zweck, J. Cryst. Growth **308**, 30 (2007).
[5]J.-H. Kim, S. C. Choi, K. S. Kim, G. M. Yang, C.-H. Hong, K. Y. Lim, and H. J. Lee, Jpn. J. Appl. Phys., Part 1 **38**, 2721 (1999).
[6]R. G. Wilson, F. A. Stevie, and C. W. Magee, *Secondary Ion Mass Spectrometry* (Wiley, New York, 1989).
[7]P. F. Miceli and C. J. Palmstrøm, Phys. Rev. B **51**, 5506 (1995).
[8]T. Metzger, R. Höpler, E. Born, S. Christiansen, M. Albrecht, H.P. Strunk, O. Ambacher, M. Stutzmann, R. Stömmer, M. Schuster, and H. Göbel, Phys. Status Solidi A **162**, 529 (1997).
[9]H. Heinke, V. Kirchner, H. Selke, R. Chierchia, R. Ebel, S. Einfeldt, and D. Hommel, J. Phys. D **34**, A25 (2001).
[10]M. W. Cho, A. Setiawan, H. J. Ko, and T. Yao, Semicond. Sci. Technol. **20**, S13 (2005).
[11]A. Boulle, R. Guinebretière, and A. Dauger, J. Appl. Phys. **97**, 073503 (2005).
[12]R. I. Barabash, W. Donner, and H. Dosch, Appl. Phys. Lett. **78**, 443 (2001).
[13]V. M. Kaganer, R. Köhler, M. Schmidbauer, R. Opitz, and B. Jenichen, Phys. Rev. B **55**, 1793 (1997).
[14]J. Als-Nielsen and D. McMorrow, *Elements of Modern X-Ray Physics* (Wiley, New York, 2001), p. 89.
[15]H. Dosch, B. W. Battermann, and D. C. Wack, Phys. Rev. Lett. **56**, 1144 (1986).
[16]A. Krost, G. Bauer, and J. Woitok, in *High Resolution X-Ray Diffraction, Optical Characterisation of Epitaxial Semiconductor Layers*, edited by G. Bauer and W. Richter (Springer, Berlin, Heidelberg, New York, 1995), pp. 287–391.
[17]J. Bläsing and A. Krost, Phys. Status Solidi A **201**, R17 (2004).
[18]V. Ratnikov, R. Kyutt, T. Shubina, T. Paskova, E. Valecha, and B. Monemar, J. Appl. Phys. **88**, 6252 (2000).